High-sensitivity spin-based electrometry with an ensemble of nitrogen-vacancy centers in diamond

Edward H. Chen, Hannah A. Clevenson, Kerry A. Johnson, Linh M. Pham, Dirk R. Englund, Philip R. Hemmer, and Danielle A. Braje

Phys. Rev. A **95**, 053417 — Published 26 May 2017

DOI: 10.1103/PhysRevA.95.053417

High-sensitivity, spin-based electrometry with an ensemble of nitrogen-vacancy centers in diamond

Edward H. Chen,[1,2,3] Hannah A. Clevenson,[1,2] Kerry A. Johnson,[2] Linh M. Pham,[2] Dirk R. Englund,[1] Philip R. Hemmer,[4] and Danielle A. Braje[2,*]

[1] *Dept. of Electrical Engineering and Computer Science, Massachusetts Institute of Technology (MIT)*
[2] *MIT Lincoln Laboratory, Lexington, MA 02420, USA.*
[3] *Present Address: HRL Laboratories, LLC. Malibu, CA 90265, USA.*
[4] *Dept. of Electrical and Computer Engineering, Texas A&M University (TAMU)*

We demonstrate a spin-based, all-dielectric electrometer based on an ensemble of nitrogen-vacancy (NV^-) defects in diamond. An applied electric field causes energy level shifts symmetrically away from the NV^-'s degenerate triplet states via the Stark effect; this symmetry provides immunity to temperature fluctuations allowing for shot-noise-limited detection. Using an ensemble of NV^-s, we demonstrate shot-noise limited sensitivities approaching 1 V/cm/$\sqrt{\text{Hz}}$ under ambient conditions, at low frequencies (<10 Hz), and over a large dynamic range (20 dB). A theoretical model for the ensemble of NV^-s fits well with measurements of the ground-state electric susceptibility parameter, $\langle k_\perp \rangle$. Implications of spin-based, dielectric sensors for micron-scale electric-field sensing are discussed.

I. INTRODUCTION

The detection of weak electric signals in low-frequency regimes is important for areas of research such as particle physics [1], atmospheric sciences [2–4], and neuroscience [5]. Commonly available ambient electrometers that rely on electrostatic induction, like field mills [6, 7] and dipole antennas [8], are physically limited in size to several tens of centimeters by the wavelength of the electric field of interest. This hinders miniaturization at frequencies below several Hertz [8–11]. Fully dielectric sensors allow sensing of electric fields without fundamental constraints on the size of the sensor and do not distort the incident field [12, 13]. Ongoing efforts to develop compact electrometers include use of the electro-optic effect within solid-state crystals [14], single electron transistors [15–17], and the energy shifts induced by electric fields of atom-based sensors such as trapped ions [18] or Rydberg atoms [19, 20]. Recently, optically-addressable electron spins in solid-state materials have played a central role in the development of quantum sensing [21, 22]. Compared with atom-based approaches that require vacuum systems, these systems allow for a higher density of spins with a reduced experimental footprint, along with other promising properties such as long room-temperature coherence times and optical accessibility for spin initialization and readout [23].

Among spin-based sensors, there has been significant progress in using ensembles of spins in diamond for sensing magnetic fields [5, 24, 25], while work in diamond-based electrometry has primarily focused on the use of single spins [26, 27]. Here, we experimentally demonstrate a spin-based, solid-state electrometer that is sensitive to the electric field induced Stark shift on an ensemble of negatively-charged nitrogen-vacancy (NV^-) color centers while being robust, to first order, to tempera-

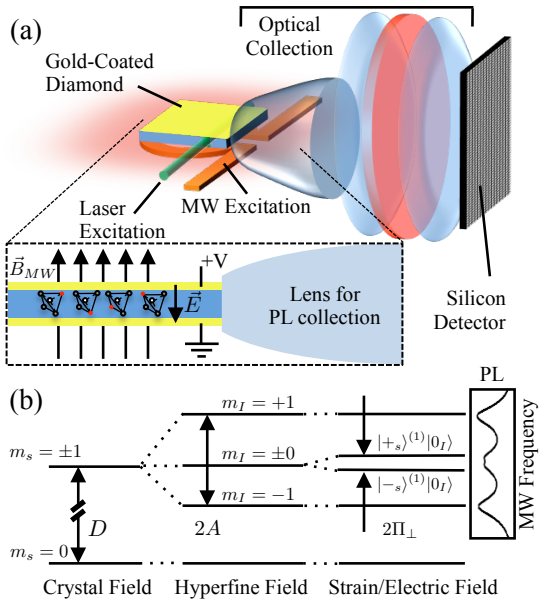

FIG. 1. (a) Diamond electrometry setup. For applying electric fields across the ensemble of NV^-s, gold electrodes were evaporated on both faces of the diamond plate (3 x 3 x 0.32 mm^3). A collimated laser beam ($\sim$ 200 µm diameter) was used to excite a single pass of NV^-s input from the edge of the diamond plate, and microwave (MW) excitation was delivered to the ensemble of NV^-s by a stripline in an 'Ω' shape patterned on a printed circuit board. *Inset* A cross-section of the experiment depicting four of the eight total NV^-orientations within an ensemble of NV^-s used for detecting electric fields. (b) Generalized diagram depicting how crystal (D), hyperfine (A), strain and the magnitude of transverse electric fields ($\Pi_\perp = \sqrt{\Pi_x^2 + \Pi_y^2}$) affect energy splitting in both the ground- and excited-state spin configurations of the NV^-. The spin labels (m_s and m_I) indicate the quantum numbers of the electronic and hyperfine states, and the two eigenstates that are sensitive to electric fields are given by: $|+\rangle_s^{(1)}|0\rangle_I$ ($m_I = +0$) and $|-\rangle_s^{(1)}|0\rangle_I$ ($m_I = -0$). The inset to the right shows the ground-state ODMR spectra of an ensemble of NV^-s.

* braje@ll.mit.edu

ture fluctuations. Our diamond-based electrometer operates at shot-noise limited sensitivities of ≈ 1 V/cm/$\sqrt{\text{Hz}}$ under ambient conditions at extremely low frequencies (0.05-10 Hz) without repetitive readout and dynamic decoupling control necessary for electrometry with single NV$^-$s [26]. By utilizing a high degree of symmetry to overcome the inhomogeneous strain and non-collinear crystallographic orientations within an ensemble of NV$^-$s, this work brings diamond-based electrometry into a regime where it has a competitive sensitivity with a clear path towards miniaturization.

NV$^-$ centers are sensitive to electric fields in both their optical ground [26] and excited triplet states [28]. Previously, electric field sensing with a single NV$^-$ was demonstrated with sensitivity down to 202 V/cm/$\sqrt{\text{Hz}}$ (891 V/cm/$\sqrt{\text{Hz}}$) at a frequency of $\sim$ 10 kHz (DC) under precisely applied magnetic fields, but the need for repetitive readout and dynamic decoupling pulse control limited that technique to frequencies in excess of 10 kHz due to the NV$^-$'s decoherence rate ($1/\text{T}_2$ where $\text{T}_2 \sim$ 0.1 ms). The device demonstrated here uses an ensemble of NV$^-$ centers in an otherwise similarly sized diamond. It is not only possible to achieve higher sensitivities (albeit over a larger volume), but it also allows for a measurement of the noise spectral density (NSD) due to low-frequency electric field fluctuations irrespective of temperature fluctuations. Furthermore, the introduced method allows for highly accurate measurement of the transverse electric susceptibility parameter, $\langle k_\perp \rangle$, of the NV$^-$'s ground state. By using this measurement modality, we expect that a diamond that is densely populated with NV$^-$s would yield a *projected* shot-noise-limited electric field sensitivity approaching 6×10^{-3} V/cm/$\sqrt{\text{Hz}}$ [29], making NV$^-$-based electrometers comparable with currently existing, room-temperature, solid-state electrometers [12, 13].

II. THEORY OF NV$^-$ ELECTROMETRY

The physical mechanism of the NV$^-$'s sensitivity to electric fields originates from its optical excited state configuration, which is a highly electric field sensitive molecular doublet (^3E). Stark shifts of the excited state cannot be measured optically under ambient conditions due to phonon-induced mixing [30]. However within each orbital of the molecular doublet, the electric field induced splitting of the $m_I = 0$ hyperfine manifold can be detected by optically detectable magnetic resonance (ODMR). Additionally, the ^3E excited-state orbital overlaps sufficiently with the ground-state molecular orbital ($^3A_2$) to also impart electric field sensitivity on the ground state spin configuration of the NV$^-$ [27].

The Hamiltonian describing both the triplet ground and excited states of the NV$^-$ share the following form [31]:

$$\hat{H}_{NV}/h = (D + d_\parallel E_\parallel)\hat{S_z}^2 + \gamma_B \vec{B} \cdot \mathbf{g} \cdot \vec{\hat{S}} + \vec{\hat{S}} \cdot \mathbf{A} \cdot \vec{\hat{I}}, \quad (1)$$

where D is the crystal field splitting (Hz), γ_B is the gyromagnetic ratio (Hz/G), $d_\parallel$ is the axial electric field dipole moment (Hz/V/cm), $E_\parallel$ is the axial electric field (V/cm), $\vec{B}$ is the magnetic field vector, $\mathbf{g}$ is the g-factor tensor, $\vec{\hat{S}}$ is the vector of electronic spin-1 Pauli operators, $\mathbf{A}$ is the hyperfine tensor, and $\vec{\hat{I}}$ is the vector of nuclear spin-1 Pauli operators. Because an electric field's effect on the NV$^-$ spin is significantly smaller than the crystal field splitting (D), the transverse electric field dependence can be considered as a perturbation to the Hamiltonian:

$$\hat{V}/h = d_\perp[\Pi_x(\hat{S}_x\hat{S}_y + \hat{S}_y\hat{S}_x) + \Pi_y(\hat{S}_x^2 - \hat{S}_y^2)], \quad (2)$$

where $d_\perp$ is the ground-state's transverse electric field dipole moment [32], Π_x and Π_y are the cartesian components of the combined strain and electric fields [33], and $\hat{S}_i$ (for $i = x, y, z$) are the spin-1 Pauli operators of the electronic spin. After diagonalizing Eqn. (1) and using

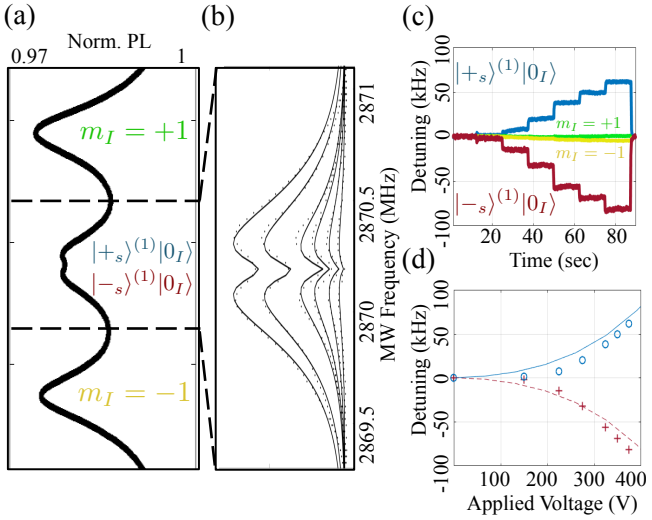

FIG. 2. (a) ODMR spectrum with correspondingly colored labels to indicate the detuning of transitions with step-wise increasing applied voltages. (b) Experimentally measured ODMR (points) at six different MW driving amplitudes overlaid with their respective numerical fits (black) using a model that accounts for an isotropic distribution of strain fields within an ensemble of NV$^-$s. The two transitions correspond to the $|-\rangle_s^{(1)}|0\rangle_I$ (red, bottom) and $|+\rangle_s^{(1)}|0\rangle_I$ (blue, top) eigenstates of the NV$^-$ triplet ground state. (c) Ground-state shifts due to incremental, step-wise electric fields applied to an ensemble of NV$^-$s at zero magnetic field. By comparing the step-wise detuning shifts of the electric field transitions with the applied voltages, it is possible to accurately deduce the ensemble average value of $\langle k_\perp \rangle = 7.0 \pm 1.1$ Hz/V/cm at a bias field of 225 Volts. (d) Data of $|+\rangle_s^{(1)}|0\rangle_I$ transition (top blue 'o') overlaid with numerical results (solid blue line). Data of $|-\rangle_s^{(1)}|0\rangle_I$ transition (bottom red '+') overlaid with numerical results (dashed red line). See Eqn. 6 for details about numerical results.

Eqn. (2) as the perturbation, there is a closed-form equation which describes the effect of electric and magnetic fields on the NV$^-$ (See Eqn. 5). The following equation accurately describes how the eigenfrequencies of a single NV$^-$change under an applied electric field ($\vec{E}$) alongside no magnetic field ($\vec{B} = 0$). Furthermore, the expression quantitatively matches the transition shifts due to a symmetric application of electric fields on all eight classes of defects within an ensemble of NV$^-$ centers:

$$f_{\pm}(\vec{B} = 0, \vec{E}) = D + k_{\parallel} E_{\parallel} \pm k_{\perp} E_{\perp} \tag{3}$$

where D is the crystal field splitting with a temperature dependence of ≈77 kHz/Kelvin [34], $k_{\parallel}$ and $k_{\perp}$ are the electric susceptibility parameters (in units of Hz/(V/cm)), and $E_{\parallel}$ and $E_{\perp}$ are the electric field amplitudes (in units of V/cm) parallel and perpendicular, respectively, to the NV$^-$ symmetry axis.

The shot-noise sensitivity to the transverse electric field (in V/cm/$\sqrt{\text{Hz}}$) limits using an ensemble of M NV$^-$s is given by the following:

$$\eta_{E_{\perp}} \approx \frac{1}{k_{\perp}} \frac{1}{C\sqrt{M\Gamma}} \frac{1}{T_2^*} \tag{4}$$

where C is the contrast of the ensemble ODMR spectra, Γ is the total photon collection rate per NV$^-$, and T_2^* is the inhomogeneous NV$^-$ coherence time. Using our experimentally measured values, we arrive at a shot-noise limit approaching $\eta_{E_{\perp}} \approx 1.0$ V/cm/$\sqrt{\text{Hz}}$ for the NV$^-$ ground state [35]. This expression shows that the sensitivity limit depends on the density of NV$^-$s in the sample, the coherence properties of the NV$^-$s, and the efficiency of photon collection.

III. EXPERIMENTAL RESULTS

The diamond measured in this work is 3.0 x 3.0 x 0.32 mm^3 in size and contains an NV$^-$ density of ∼1 ppb produced during the chemical vapor growth process. The two square faces on which the electrodes were evaporated have (100) crystallographic orientations (See Fig. 1), and thus the applied electric field produces an equal projection onto all eight orientations of NVs within the ensemble. We measured ODMR of the ensemble of NV$^-$s using continuous-wave (CW) laser and microwave excitation from the side and bottom, respectively.

To account for the distribution of strain magnitudes and angles within the ensemble of NV$^-$s, we use the (2,1) Gamma probability distribution as an ansatz for the magnitude distribution, and assume a uniform and isotropic angular distribution [36]. This model accounting for the isotropic distribution of strain accurately fits the experimental data (See Fig. 2b). We also simulated the expected electric field induced shift on the ensemble average of NV$^-$s in Fig. 2c using an estimated distribution of strain. The simulated results match well with the step-wise increase in electric field; this agreement validated the use of this method for accurately scaling the measured shift in frequency to the reported noise floor of the noise spectral density (See Figures 2c,d).

To detect a shift in NV$^-$ transition frequencies of the NV$^-$ensemble due to an external electric field, the magnetic field along the NV$^-$ axes must be significantly weaker than the internal electric or strain fields. The maximum electric field sensitivity is achieved at zero magnetic field, but at the expense of vector sensitivity [26]. Additionally, the shot-noise limited sensitivity given by Eqn. 4 can be optimized by controlling the laser and microwave excitation powers.

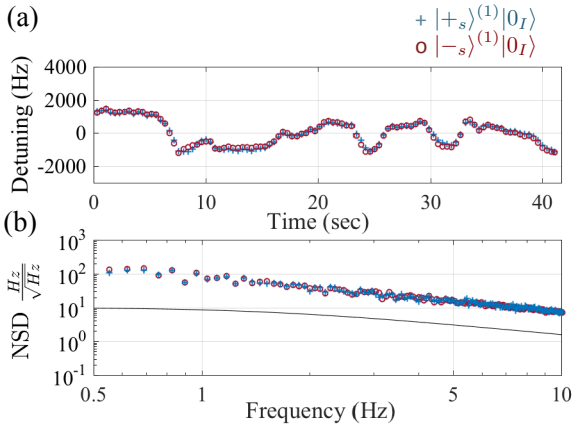

FIG. 3. Measurements taken at 1.8 W laser excitation with a high-stability bias voltage of 225 Volt. (a) Time trace of both lock-in-amplifier channels monitoring frequency detuning of ensemble states $|+\rangle_s^{(1)}|0\rangle_I$ (blue '+') and $|-\rangle_s^{(1)}|0\rangle_I$ (red 'o') in units of transition frequency noise per $\sqrt{\text{Hz}}$. (b) Noise spectral density (NSD) of both channels. The noise floor of the red (blue channel is calculated to be equivalent to 12.6 ± 6.4 (13.4 ± 7.4) V/cm/$\sqrt{\text{Hz}}$, assuming the noise is entirely attributed to electric field fluctuations. The electric field sensitivity estimated by the shot-noise limit is given by the black line (1.2 ± 0.1 V/cm/$\sqrt{\text{Hz}}$).

We measured two electric and strain sensitive transition frequencies (denoted as $m_I = \pm 0$) simultaneously at a rate inversely proportional to the time constant of the home-built lock-in instrumentation [37]. Although only the two transitions are monitored, the shift in frequencies correspond to an average shift due to the entire ensemble. The inhomogeneous strain typically found in the ensemble is indistinguishable from an inhomogeneous distribution of electric fields. Using a bias electric field beyond the average strain of the ensemble of NV$^-$ centers, the shift of the $m_I = \pm 0$ (See Fig. 1 for notation) transitions

become linearly sensitive to electric fields, while the transitions, $m_I = \pm 1$, remain relatively insensitive to electric fields due to the quadrupole field of the host nuclear ^{14}N spin (See Fig.2d).

Figure 3 presents the resulting sensitivity measurements. A maximum electric field sensitivity of the ensemble of NV$^-$s was achieved with an incident laser power of 1.8 W. However, the high input laser ($\sim$30 μW/μm^2) powers required to saturate the photoluminescence from the NV$^-$s contributes to greater temperature fluctuations in the diamond. In a simultaneous time trace of the $m_I = \pm 0$ transitions, there are significant correlated shifts due to the temperature fluctuations (See Fig. 3a). The noise-spectral densities (NSD) of the two time traces indicate $1/f$-type noise, which is consistent with the source of the noise being due to temperature fluctuations. The noise floors of both channels are more than a factor of 10$\times$ greater than the shot-noise limit (See Fig. 3b).

The temperature fluctuations are separated from the electric field fluctuations using the temperature-dependent, correlated shifts of the D parameter (See Eqn. 3). The sum of the time traces corresponds to the temperature fluctuations while the difference of the time traces corresponds to the electric field fluctuations. The NSD of the resulting sum and differences shows temperature fluctuations of 2.4 ± 1.2 mK/$\sqrt{\text{Hz}}$ and electric field fluctuations of 1.6 ± 1.2 V/cm/$\sqrt{\text{Hz}}$, respectively (See Fig. 4). Thus, our method shows a shot-noise-limited electric-field sensitivity that is approximately 8$\times$ improved over a measurement without deconvolution with temperature fluctuations.

IV. DISCUSSION

We have demonstrated sensing of electric fields with an ensemble of NV$^-$s below 1 Hz with sensitivities approaching 1 V/cm/$\sqrt{\text{Hz}}$. In spite of large temperature variations, inhomogeneous distribution of strain and non-collinear orientations, our measurement technique allows for accurate measurements of the ensemble strain distribution and the ensemble average of the transverse electric susceptibility, $k_\perp$; both of which are needed to accurately measure low-frequency electric fields.

NV$^-$-based sensing lends itself to imaging electric fields at or below the optical diffraction limit [38–40]. We anticipate that the use of low-strain nanodiamonds with our demonstrated zero-magnetic field regime would enable simultaneous monitoring of both temperature [41] and electric fields [26]. To the best of our knowledge, nanodiamonds with low-strain ($<$ 200 kHz) are not yet available despite the tremendous progress in improving the electronic coherence within such nano-scale structures [42, 43]. Such low-strain nanodiamonds with high densities of NV$^-$s would be beneficial for *in vitro* biological studies [44, 45] and microelectronic diagonistics [46]. Finally, due to the many combinations of host materials and defects, there is significant potential in discovering defects within two- and three-dimensional materials that would further improve upon existing electronic spin-based electrometers [47, 48].

In this work, we have demonstrated a factor of more than 200x improvement over previous demonstrations using a single NV$^-$. The sensitivity may be further improved by using a diamond with 1000x higher densities of NV$^-$s [5], improving the photon collection efficiency by another 10-100 times by patterning the diamond surface to overcome the confinement due to total internal reflection [49, 50], and implementing pulsed control techniques to avoid power-broadening of the transitions [51–54]. Such readily accessible material and setup improvements could improve the shot-noise limited electric field sensitivity to 6×10^{-3} V/cm/$\sqrt{\text{Hz}}$. Additional coherent control on either the surrounding electron [55, 56] or nuclear spins [57–59] in diamond would further improve the sensitivity by reducing the broadening of the transition line width. MW field inhomogeneities that are typically more problematic for pulsed techniques would benefit from recently proposed methodologies for generating robust pulse sequences [60]. Other promising directions for spin-based sensing involve all-optical techniques in diamond for electrometry [61].

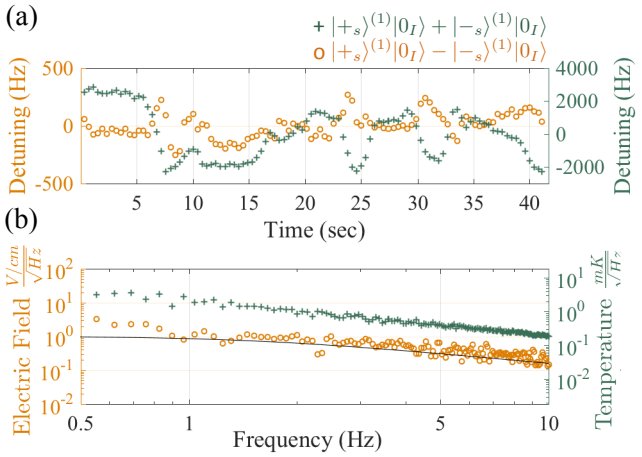

FIG. 4. Identical experimental measurements as in Fig. 3 except the analysis takes advantage of the experimental methodology for deconvolving fluctuations from temperature and electric fields. (a) Time trace of the difference (orange 'o', electric field) and sum (green '+', temperature) of the lock-in-amplifier channels from Fig. 3. (b) NSD on the time-trace difference (sum) of the two channels, which corresponds to a sensitivity of 1.6 ± 1.2 V/cm/$\sqrt{\text{Hz}}$ (2.4 ± 1.2 mK/$\sqrt{\text{Hz}}$) due the transverse electric field (temperature) fluctuations. The sum of the two correlated channels yields a shot-noise sensitivity limit of 0.9 ± 0.1 V/cm/$\sqrt{\text{Hz}}$ (black line), which is $\sqrt{2}$ times lower than that of the individual channels as seen in Fig. 3b.

ACKNOWLEDGMENTS

Acknowledgements: The authors would like to thank Paola Cappellaro, John Barry, John Cortese, Colin Bruzewicz, Florian Dolde, Carson Teale, Christopher McNally, Christopher Foy, Xiao Wang, Peter Murphy, Sinan Karaveli, Jeremy Sage, and Jonathon Sedlack for fruitful discussions. E.H.C. and H.C. were supported by NASA's Office of Chief Technologist on the Space Technology Research Fellowship. D.E. acknowledges support by the Air Force Office of Scientific Research PECASE, supervised by Dr. Gernot Pomrenke.

This material is based upon work supported by the Assistant Secretary of Defense for Research and Engineering under Air Force Contract No. FA8721-05-C-0002 and/or FA8702-15-D-0001. Any opinions, findings, conclusions or recommendations expressed in this material are those of the author(s) and do not necessarily reflect the views of the Assistant Secretary of Defense for Research and Engineering.

[1] S. Sharma, C. Hovde, and D. H. Beck, SPIE Proceedings **9755** (2016), 10.1117/12.2211910.

[2] F. J. Merceret, J. G. Ward, D. M. Mach, M. G. Bateman, and J. E. Dye, Journal of Applied Meteorology and Climatology **47**, 240 (2008).

[3] F. Simoes, R. Pfaff, J.-J. Berthelier, and J. Klenzing, Space Science Reviews **168**, 551 (2012).

[4] K. Mezuman, C. Price, and E. Galanti, Environmental Research Letters **9**, 124023 (2014).

[5] J. F. Barry, M. J. Turner, J. M. Schloss, D. R. Glenn, Y. Song, M. D. Lukin, H. Park, and R. L. Walsworth, Proceedings of the National Academy of Sciences (2016).

[6] A. Fort, M. Mugnaini, V. Vignoli, S. Rocchi, F. Perini, J. Monari, M. Schiaffino, and F. Fiocchi, Ieee Transactions on Instrumentation and Measurement **60**, 2778 (2011).

[7] P. S. Riehl, K. L. Scott, R. S. Muller, R. T. Howe, and J. A. Yasaitis, Journal of microelectromechanical systems **12**, 577 (2003).

[8] R. F. Harrington, J. Res. Nat. Bur. Stand **64**, 1 (1960).

[9] L. J. Chu, Journal of Applied Physics **19**, 1163 (1948).

[10] J. Chubb, Journal of Electrostatics **78**, 1 (2015).

[11] R. Barr, D. L. Jones, and C. J. Rodger, Journal of Atmospheric and Solar-Terrestrial Physics **62**, 1689 (NOV-DEC 2000).

[12] A. A. Savchenkov, W. Liang, V. S. Ilchenko, E. Dale, E. A. Savchenkova, A. B. Matsko, D. Seidel, and L. Maleki, AIP Advances **4**, 122901 (2014).

[13] J. E. Toney, *Lithium Niobate Photonics* (Artech House, 2015).

[14] S. T. Vohra, F. Bucholtz, and A. D. Kersey, Optics Letters **16**, 1445 (1991).

[15] J. Lee, Y. Zhu, and A. Seshia, Journal of Micromechanics and Microengineering **18**, 025033 (2008).

[16] J. Vincent, V. Narayan, H. Pettersson, M. Willander, K. Jeppson, and L. Bengtsson, Journal of applied physics **95**, 323 (2004).

[17] C. Neumann, C. Volk, S. Engels, and C. Stampfer, Nanotechnology **24**, 444001 (2013).

[18] C. D. Bruzewicz, J. M. Sage, and J. Chiaverini, Physical Review A **91**, 041402 (2015).

[19] A. Osterwalder and F. Merkt, Physical Review Letters **82**, 1831 (1999).

[20] J. A. Sedlacek, A. Schwettmann, H. Kübler, R. Löw, T. Pfau, and J. P. Shaffer, Nature Physics **8**, 819 (2012).

[21] D. D. Awschalom, L. C. Bassett, a. S. Dzurak, E. L. Hu, and J. R. Petta, Science **339**, 1174 (2013).

[22] C. Degen, F. Reinhard, and P. Cappellaro, arXiv preprint arXiv:1611.02427 (2016).

[23] V. Acosta and P. Hemmer, MRS Bulletin **38**, 127 (2013).

[24] H. Clevenson, M. E. Trusheim, C. Teale, T. Schröder, D. Braje, and D. Englund, Nature Physics **11**, 393 (2015).

[25] K. Fang, V. Acosta, C. Santori, Z. Huang, K. Itoh, H. Watanabe, S. Shikata, and R. Beausoleil, Physical Review Letters **110** (2013), 10.1103/PhysRevLett.110.130802.

[26] F. Dolde, H. Fedder, M. W. Doherty, T. Nöbauer, F. Rempp, G. Balasubramanian, T. Wolf, F. Reinhard, L. C. L. Hollenberg, F. Jelezko, and J. Wrachtrup, Nature Physics **7**, 459 (2011).

[27] M. W. Doherty, J. Michl, F. Dolde, I. Jakobi, P. Neumann, N. B. Manson, and J. Wrachtrup, New Journal of Physics **16**, 063067 (2014).

[28] P. Tamarat, T. Gaebel, J. Rabeau, M. Khan, A. Greentree, H. Wilson, L. Hollenberg, S. Prawer, P. Hemmer, F. Jelezko, *et al.*, Physical review letters **97**, 083002 (2006).

[29] See Appendix for this projected sensitivity using values from recent magnetometry experiments [5].

[30] T. Plakhotnik, M. W. Doherty, J. H. Cole, R. Chapman, and N. B. Manson, Nano Letters **14**, 4989 (2014).

[31] M. W. Doherty, N. B. Manson, P. Delaney, F. Jelezko, and L. C. L. Hollenberg, Physics Reports **528**, 1 (2013).

[32] See [27] for the relationship between electric-dipole moment, $d_\perp$ and the electric susceptibility, $k_\perp$.

[33] See Fig. 7 for the differences and similarities in using the ground and excited states of the NV^- for electrometry.

[34] X.-D. Chen, C.-H. Dong, F.-W. Sun, C.-L. Zou, J.-M. Cui, Z.-F. Han, and G.-C. Guo, Applied Physics Letters **99**, 161903 (2011).

[35] $k_\perp^{225\text{ V Bias}} = 7\text{ Hz/V/cm}, C \approx 0.02, 1/T_2^* \approx 4 \times 10^5$ Hz, $M \approx 5 \times 10^9, \gamma \approx 100$ photons per second.

[36] See Appendix for an analysis considering the isotropic distribution of strain with an ensemble of NV^-s.

[37] See Appendix for a description of the technical details of the setup.

[38] E. H. Chen, O. Gaathon, M. E. Trusheim, and D. Englund, Nano Letters **13**, 2073 (2013).

[39] M. Pfender, N. Aslam, G. Waldherr, P. Neumann, and J. Wrachtrup, Proceedings of the National Academy of Sciences **111**, 14669 (2014).

[40] W. W.-W. Hsiao, Y. Y. Hui, P.-C. Tsai, and H.-C. Chang, Accounts of Chemical Research **49**, 400 (2016).

[41] G. Kucsko, P. C. Maurer, N. Y. Yao, M. Kubo, H. J. Noh, P. K. Lo, H. Park, and M. D. Lukin, Nature **500**,

54 (2013).
[42] H. S. Knowles, D. M. Kara, and M. Atatüre, Nature Materials **13**, 21 (2014).
[43] M. E. Trusheim, L. Li, A. Laraoui, E. H. Chen, H. Bakhru, T. Schröder, O. Gaathon, C. A. Meriles, and D. Englund, Nano Letters **14**, 32 (2014).
[44] I. Řehoř, J. Šlegerová, J. Havlík, H. Raabová, J. Hývl, E. Muchová, and P. Cígler, in *Carbon Nanomaterials for Biomedical Applications*, Springer Series in Biomaterials Science and Engineering No. 5, edited by M. Zhang, R. R. Naik, and L. Dai (Springer International Publishing, 2016) pp. 319–361.
[45] S. Karaveli, O. Gaathon, A. Wolcott, R. Sakakibara, O. A. Shemesh, D. S. Peterka, E. S. Boyden, J. S. Owen, R. Yuste, and D. Englund, Proceedings of the National Academy of Sciences , 201504451 (2016).
[46] A. Nowodzinski, M. Chipaux, L. Toraille, V. Jacques, J.-F. Roch, and T. Debuisschert, Microelectronics Reliability **55**, 1549 (2015).
[47] C. Freysoldt, B. Grabowski, T. Hickel, J. Neugebauer, G. Kresse, A. Janotti, and C. G. Van de Walle, Reviews of Modern Physics **86**, 253 (2014).
[48] T. T. Tran, C. Zachreson, A. M. Berhane, K. Bray, R. G. Sandstrom, L. H. Li, T. Taniguchi, K. Watanabe, I. Aharonovich, and M. Toth, Physical Review Applied **5**, 034005 (2016).
[49] A. W. Schell, T. Neumer, Q. Shi, J. Kaschke, J. Fischer, M. Wegener, and O. Benson, Applied Physics Letters **105**, 231117 (2014).
[50] L. Li, E. H. Chen, J. Zheng, S. L. Mouradian, F. Dolde, T. Schröder, S. Karaveli, M. L. Markham, D. J. Twitchen, and D. Englund, Nano Letters **15**, 1493 (2015).
[51] J. S. Hodges, N. Yao, D. Maclaurin, C. Rastogi, M. Lukin, and D. Englund, Physical Review A **87**, 032118 (2013).
[52] D. M. Toyli, C. F. de las Casas, D. J. Christle, V. V. Dobrovitski, and D. D. Awschalom, Proceedings of the National Academy of Sciences **110**, 8417 (2013).
[53] P. Neumann, I. Jakobi, F. Dolde, C. Burk, R. Reuter, G. Waldherr, J. Honert, T. Wolf, A. Brunner, J. H. Shim, D. Suter, H. Sumiya, J. Isoya, and J. Wrachtrup, Nano Letters **13**, 2738 (2013).
[54] P. Jamonneau, M. Lesik, J. Tetienne, I. Alvizu, L. Mayer, A. Dréau, S. Kosen, J.-F. Roch, S. Pezzagna, J. Meijer, *et al.*, Physical Review B **93**, 024305 (2016).
[55] P. Cappellaro, Physical Review A **85**, 030301 (2012).
[56] C. Bonato, M. S. Blok, H. T. Dinani, D. W. Berry, M. L. Markham, D. J. Twitchen, and R. Hanson, Nature nanotechnology **11**, 247 (2016).
[57] M. Hirose and P. Cappellaro, Nature **532**, 77 (2016).
[58] T. Unden, P. Balasubramanian, D. Louzon, Y. Vinkler, M. B. Plenio, M. Markham, D. Twitchen, A. Stacey, I. Lovchinsky, A. O. Sushkov, *et al.*, Physical Review Letters **116**, 230502 (2016).
[59] H. A. Clevenson, E. H. Chen, F. Dolde, C. Teale, D. Englund, and D. Braje, Phys. Rev. A **94**, 021401 (2016).
[60] D. Farfurnik, A. Jarmola, L. M. Pham, Z.-H. Wang, V. V. Dobrovitski, R. L. Walsworth, D. Budker, and N. Bar-Gill, Physical Review B **92**, 060301 (2015).
[61] A. Wickenbrock, H. Zheng, L. Bougas, N. Leefer, S. Afach, A. Jarmola, V. M. Acosta, and D. Budker, Applied Physics Letters **109**, 053505 (2016).

Appendix A: Appendix

1. Addressing an ensemble of NV$^-$s

A diagram showing four of the eight possible NV$^-$ orientations found with a diamond containing an ensemble of NV$^-$s (See Fig. 5).

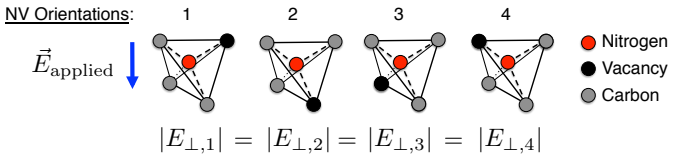

FIG. 5. Applied electric field with respect to the eight orientations of NVs in the ensemble.

2. Sensitivity approaching $\frac{\text{mV}}{\sqrt{\text{Hz}}}$

Using Eqn. 4 in the main text, we expect a shot-noise-limited sensitivity approaching $6 \times 10^{-3} \frac{\text{V/cm}}{\sqrt{\text{Hz}}}$ using photocurrent values of 10 mW ($n\gamma = 62 \times 10^{15}$ eV/sec $\times$ 1 photon/1.9eV $= 3 \times 10^{16}$ photon/sec) as typically seen with ensemble NV$^-$ measurements for magnetometry experiments [5], a transverse electric susceptibility of $k_\perp = 17 \frac{Hz}{\text{V/cm}}$, line width ($\Delta f$) of 1 MHz, and contrast(C) of 0.05.

3. Full energy transition expression

Using second-order, degenerate perturbation theory, we derive the microwave transition frequencies between the eigenstates split by transverse electric fields:

$$\omega_\pm(\vec{E},\vec{B}) = D + k_\parallel E_\parallel + 3\frac{(\gamma_B B_\perp)^2}{2D} \pm\sqrt{B_\parallel^2 + E_\perp^2 - \frac{1}{2}\sqrt{B_\parallel^2 + E_\perp^2}\frac{B_\perp^2}{2D} sin(\alpha)cos(\beta) + (\frac{B_\perp^2}{2D})^2} \tag{A1}$$

where $\tan(\alpha) = E_\perp/B_\parallel$, $\beta = 2\phi_B + \phi_E$, $\tan(\phi_B) = B_y/B_x$, $\tan(\phi_E) = E_y/E_x$, $B_\perp \equiv \sqrt{B_x^2 + B_y^2}$, and $E_\perp \equiv \sqrt{E_x^2 + E_y^2}$.

The equation which describes the ensemble ODMR spectrum is given by:

$$I_{\pm}(f) = 1 - \frac{1}{24\pi}\int_0^{2\pi}\int_0^{\pi}\int_0^{\infty} \frac{C_o\ \mathbf{P}(x)}{4\left(\frac{f-(D_o \pm k_\perp E_o x\sin(\theta))}{\Delta f_o}\right)^2 + 1} x^2\sin(\theta)dxd\theta d\phi \tag{A2}$$

where f is the frequency of the applied MW field, C_o is the ensemble average of the ODMR contrast, D_o is the ensemble average of the crystal field, $\mathbf{P}(x) = xe^{-x}$ is the (2,1) Gamma probability distribution of the strain magnitude, E_o is the ensemble average of the strain magnitude, Δf_o is the full-width half-maximum of single-NV line-widths, θ denotes the strain vector's altitude angle away from the NV$^-$ symmetry axis, and ϕ is the strain vector's azimuthal angle.

4. Zero-ing of magnetic field using gradient descent

It is possible to zero the magnetic field using gradient descent because the overlap of the $m_I = \pm 1$ transitions of all eight orientations of NV$^-$s has a contrast that varies smoothly with respect to applied small magnetic fields. By taking local gradients of the contrast at each magnetic field setting (B_x, B_y and $B_\parallel$) followed by successively smaller step sizes, we find the setting of $\vec{B}$ that achieves the globally maximum ODMR contrast and hence a zero magnetic field.

5. Digital Lock-In Amplifier Implementation

Using an FPGA high speed DAC, our system contains both the waveform generation and lock-in detection to perform readout of the optical signals from the diamond. The MW waveform sent to the diamond is generated digitally in the FPGA by direct-sampling with a high-speed DAC (2.4 Giga-samples, 3rd nyquist zone), which significantly simplifies the RF hardware and allows generation of arbitrary waveforms. Control is performed by a Linux based Python TCP/IP server running on the Zynq's ARM processor that interfaces to MATLAB on the control PC.

6. Bandwidth limitations of the NV-based electrometer

The mechanism that determines the NV spin's sensitivity to high frequency electric fields at room temperature is limited by the spin-dependent readout rate. This rate is limited by the intersystem crossing process which is weakly temperature dependent due to its non-spin conserving property, and is ≈1/300 ns. Due to current experimental constraints such as limited photon collection efficiency and a limited bandwidth of the photodiode given the large dynamic range needed, the time constant on the LIA can then be set to match the bandwidth of the NV electrometer's spin readout of ≈3 MHz. Higher detection bandwidths can be achieved using single-shot spin readout at cryogenic temperatures.

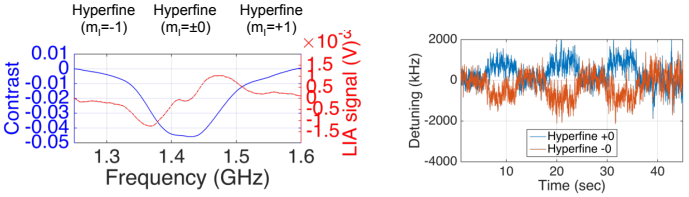

FIG. 6. Excited-state ODMR spectra measured on an NV$^-$ ensemble at zero magnetic field. Excited-state shifts due to pulsed electric fields applied to an NV$^-$ ensemble at zero magnetic field. The sensitivity of this measurement approaches $300\frac{\mathrm{V/cm}}{\sqrt{\mathrm{Hz}}}$.

	Ground State	Excited State
Lande' g factor (g)	2	2
Lifetime (T_1)	milliseconds	nanoseconds
Crystal Field Splitting (D)	2.8 GHz	1.4 GHz
N^{14} Hyperfine splitting (A)	2 MHz	40 MHz
Transverse field Sensitivity (d)	17 Hz / (V/cm)	~400 Hz / (V/cm)

FIG. 7. Table outlining the major differences between the ground and excited state of the NV$^-$ for electric field sensing.

7. Excited-state optically detected magnetic resonance

The spin physics of the NV$^-$'s excited state is identical with the NV$^-$'s ground state at temperatures above approximately 50 Kelvin [25]. For purposes of sensing electric fields, the excited state is expected to be significantly less effective despite having 20 × greater transverse field sensitivity. This is attributed to shorter optical spontaneous lifetime (12 ns) and smaller ODMR contrast in the excited state. This analysis can be validated by substituting values from Fig. 7 into Eqn. 4.